Journal of Sol-Gel Science and Technology (2020) 95:180–189
https://doi.org/10.1007/s10971-020-05296-x

ORIGINAL PAPER: NANO-STRUCTURED MATERIALS (PARTICLES, FIBERS, COLLOIDS, COMPOSITES, ETC.)

Effect of preparation conditions on physical properties of manganese oxide thin films

Abbas Bahadori[1] · Hamid Rezagholipour Dizaji[1] · Nafiseh Memarian[1] · Maryam Aliannezhadi[1]

Received: 20 December 2019 / Accepted: 11 April 2020 / Published online: 29 April 2020

Abstract

Nanostructured manganese oxide (Mn_2O_3) thin films were synthesized by spin coating method. The effect of preparation conditions, such as calcination temperature, rotation speed, as well as solution aging time on structural, morphological, and optical properties of the samples were investigated. The phase of the grown films changed from amorphous to orthorhombic by applying the calcination temperature beyond 400 °C. At low calcination temperature, agglomerations of the particles happened and no uniform structure formed. Furthermore, the results indicated that employing higher rotation speeds led to decrement of the samples crystallinity. Aging the solution did not change the absorption edge of the samples. However, the optical transmittance of the samples decreased by about 10 percent.

Graphical Abstract

Surface FESEM image of seven layer Mn_2O_3 thin film calcined at 500 °C

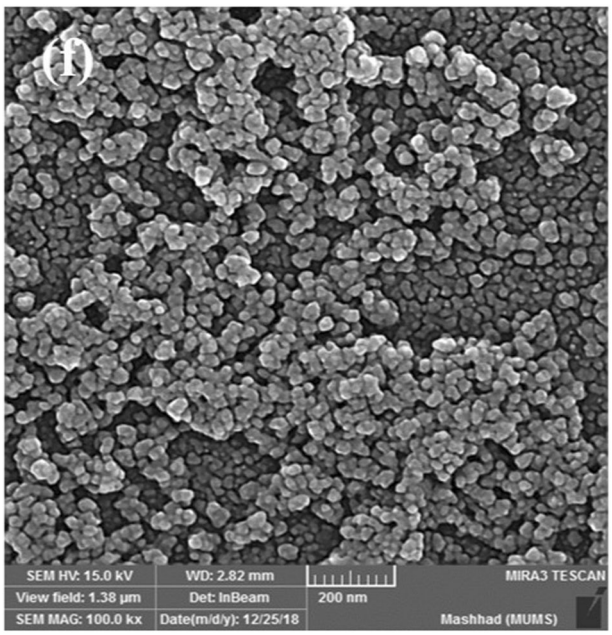

✉ Hamid Rezagholipour Dizaji
hrgholipour@semnan.ac.ir

[1] Faculty of Physics, Semnan University, P.O. Box: 35195-363, Semnan, Iran

Keywords Manganese oxide · Spin coating · Nanostructured thin films · Optical properties · Structural properties

Highlights

- Mn_2O_3 thin films have been prepared by sol-gel spin coating technique.
- Structural, morphological, and optical properties of Mn_2O_3 thin films have been studied.
- The effects of calcination temperature as well as rotation spin in spinning process have been investigated.
- The effect of solution aging on physical properties of the Manganese oxide thin films has been studied.

1 Introduction

Nanostructured transition metal oxide thin films have attracted the attention of researchers and industry due to their unique physical and chemical properties [1–4]. Their special properties are because of the finite size and high surface to volume ratio. Among these nanomaterials, manganese oxide is particularly interested due to its non-toxicity, low prices, and availability. Manganese oxide nanostructures have a wide areas of applications in optics, electronics, and chemistry [5]. These nanostructures are widely used in electrochromic devices [6, 7], lithium-ion batteries [8–10], sensors [11, 12], high-efficiency chemical electrodes [13], electrochemical capacitors [9, 14], and so on.

Different methods can be used to fabricate manganese oxide nanostructures such as hydrothermal [15] and sol–gel [16]. Sol–gel has some advantages such as low processing temperatures, high chemical homogeneity, and the ability to control the size and morphology of nanostructures. In addition, their thin films can be produced by several methods like pulsed laser deposition [17], vacuum evaporation [18], chemical vapor deposition [19], spray pyrolysis [20], chemical bath deposition [21], atomic layer deposition [22], spin-coating [23], and sol–gel method [24]. Among these coating methods, spin-coating is a promising method that attracted the attention of researches due to low cost, fast operating, easily controllable coating variables, homogeneity, and uniformity of the products [25].

Manganese has different oxidation states and it can be converted to Mn^{2+}, Mn^{3+}, and Mn^{+4} ions to form MnO, Mn_2O_3, MnO_2, Mn_2O_7, Mn_3O_4 [26]. Various crystallographic phases of α, β, δ, λ, and γ have been reported for manganese oxide nanostructures in the literature [27]. Morphology and crystallographic forms of manganese oxide nanostructures strongly depends on the preparation conditions. Recently, α-MnO_2 nanowires prepared by the hydrothermal method are reported for electromagnetic shielding [28]. Augustin et al have studied the effect of calcination temperature and O_2 and Ar flows on manganese oxide formed by chemical precipitation method [29]. According to their results, the calcination temperature and the presence of gas flow significantly affects crystalline phase, lattice parameters, and crystallite size of MnO_x species. They have found the best electrochemical performance for α-Mn_2O_3 phase through the linear sweep voltammetry measurements. Very recently, Fang et al. have reported the effect of Tween surfactant on morphology and electrical conductivity of Mn_2O_3 nanostructures formed by the solvothermal method. Their results have revealed the formation of different morphologies and electrical conductivity improvement upon adding the surfactant [30].

Furthermore, the MnO_2–ZnO thin films prepared by dip-coating method on glass substrates have been reported and the effect of different zinc concentration has been investigated [31]. In addition, tetrapropylammonium manganese oxide thin films have been formed onto nickel foils by dip-coating technique showing interesting capacitive behavior, good reversibility, and cycling stability [32]. Moreover, MnO_2 films deposited by sputtering at different annealing temperature have been studied [33]. The results have shown the annealing temperature as an important parameter causing the appearance of β-MnO_2 and well crystallized β-Mn_2O_3 phases at 450 °C and 600 °C, respectively. Also, the effect of calcination temperature on self-assembled MnO_2 thin films prepared directly on Ni-coated PET substrates has been investigated by Pang et al. [34]. According to their results, calcination temperature had a significant effect on the surface morphology, and the charge capacities increased reasonably with increasing the calcination temperatures up to 200 °C. In another research, spin coating of different commercial powders with different manganese oxide phases has been studied [35]. The effects of calcination temperature on morphological, structural, and electrochemical properties, and oxygen/hydrogen evolutions have been investigated. The results have shown that the MnO_2 sample with amorphous structure had turned to α-Mn_2O_3 crystalline phase after calcination at 500 °C for 2 h. Furthermore, the results indicated that spin-coated samples had better oxygen/hydrogen evolution performance compared to electrodeposited films.

To the best of our knowledge, the effect of calcination temperature on structural, morphological, and optical properties of manganese oxide thin films prepared by sol–gel spin coating method has not been considered until now. Therefore, the focus of the present research has been made on the effect of calcination temperature on the

Table 1 sample coding for different deposition and calcination conditions

Sample	Rotation speed (rpm)	Number of deposited layers	Calcination temperature (°C)
S^5_{400}	3000	5	400
S^5_{450}	3000	5	450
S^6_{400}	3000	6	400
S^6_{450}	3000	6	450
S^6_{500}	3000	6	500
S^7_{500}	3000	7	500
S_{2000}	2000	6	500
S_{2500}	2500	6	500
S_{3000}	3000	6	500
S_{4000}	4000	6	500

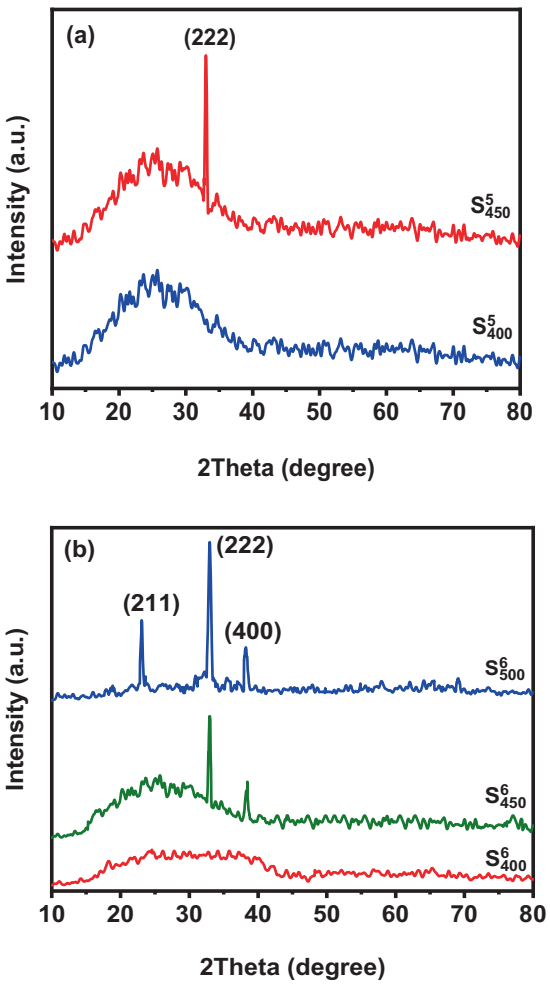

Fig. 1 XRD patterns of manganese oxide thin films for samples calcined at different temperatures; **a** five times deposition for $S^5_{400}$and S^5_{450}, and **b** six times deposition for S^6_{400}, S^6_{450}, and S^6_{500}

physical properties of manganese oxide thin films by using sol–gel spin coating method. For this purpose, three annealing temperatures of 400, 450, and 500 °C have been considered to find the optimum calcination temperature. In addition, rotation spin in spinning process, as well as the effect of solution aging on physical properties of the manganese oxide thin films, have been studied.

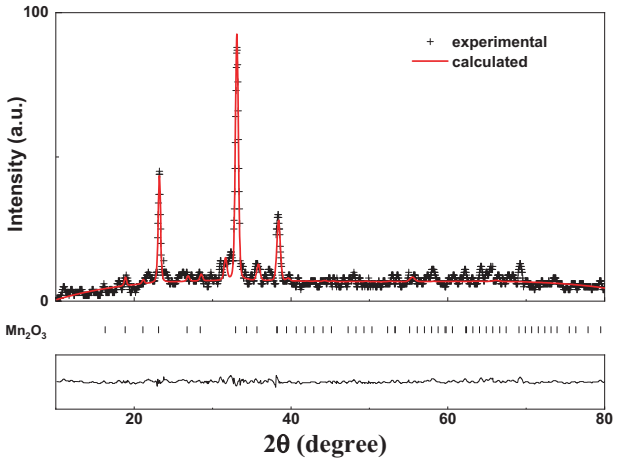

Fig. 2 Experimental and calculated (Rietveld analysis) XRD pattern of S^6_{500} sample, plus: experimental data; solid line: Rietveld fit. The bar sequence shows the position of peaks according to the lattice parameter value. Bottom panel indicates the difference between calculated curve and experimental data

2 Experimental

Mn_2O_3 thin films were prepared by using sol–gel spin coating method. Typically, a certain amount of manganese acetate ($C_6H_9MnO_6{\cdot}4H_2O$, Merck, 98%) was dissolved in 6 ml mono-ethanolamine (C_2H_7NO, Merck, 98%) with a molar ratio of 1:1. Then, 10 ml 2-methoxyethanol ($CH_3OCH_2CH_2OH$, Merck, 98%) was added. The final concentration of manganese acetate was 0.5 M. Then the mixture was stirred for 3 h by a magnetic stirrer at 80 °C. pH of the resulting solution was 7. After aging the solution for 24 h, manganese oxide thin films were deposited on precleaned soda-lime glass substrates by spin coating technique at different rotation speeds (2000–4000 rpm) for 30 s. The spin coating apparatus used in the present investigation can rotate up to 9000 rpm with the accuracy of 5 rpm. A rotary pump was used during layer deposition to avoid substrate separation while the deposition process was going on.

The wet films were dried in an oven at 100 °C for 30 min. This process was repeated several times to have thin films of different layer numbers with desirable physical properties. Finally, the films were calcined at different temperatures (400–450–500 °C) in the presence of oxygen flux (grade 6) by tube furnace. The resulting samples are labeled as listed in Table 1. In addition, the effect of solution aging period was investigated, and samples were labeled as non-aged, 15 d, 30 d, and 45 d,

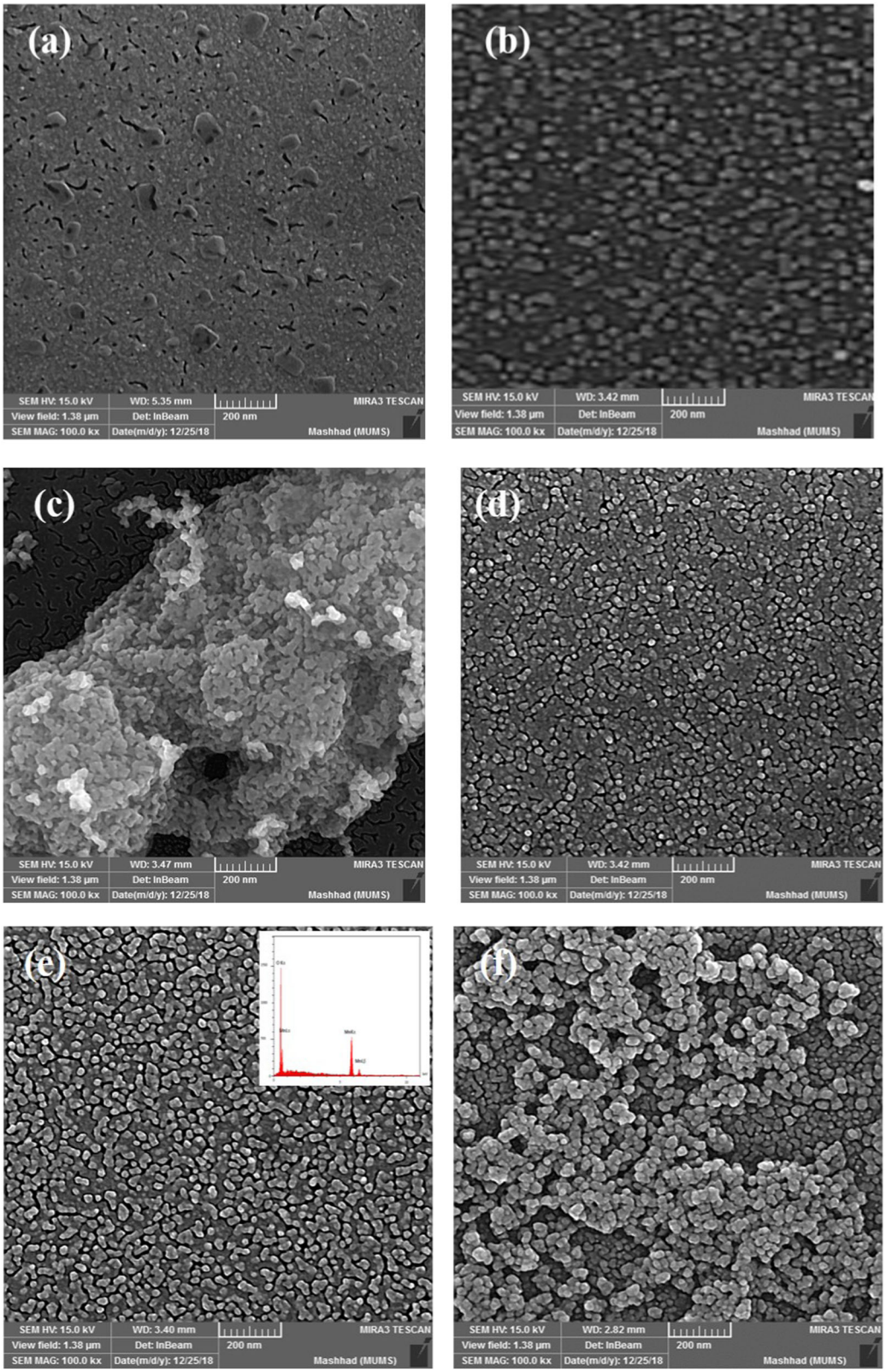

Fig. 3 Surface FESEM images of **a** S^5_{400}, **b** S^5_{450}, **c** S^6_{400}, **d** S^6_{450}, **e** S^6_{500}, and **f** S^7_{500}. The insets in **e** is the EDX analysis of that sample

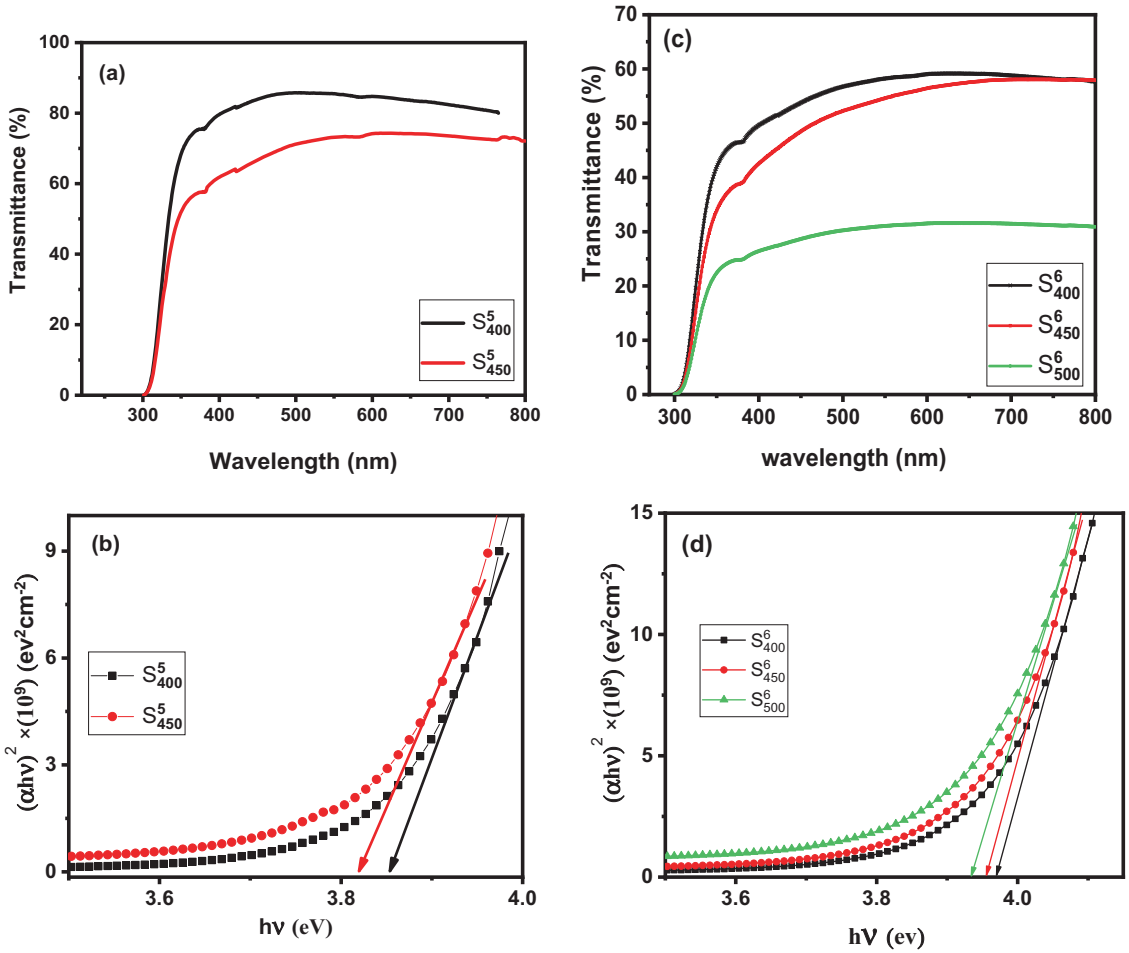

Fig. 4 Optical transmittance and Tauc's plot of samples with different calcination temperatures, **a**, **c** for S^5_{400} and S^5_{450} samples, and **b**, **c** for S^6_{400}, S^6_{450}, S^6_{500} samples, respectively

for fresh solution, 15 days, 30 days, and 45 days aged solutions, respectively.

The crystalline structure of the films was analyzed by X-ray diffraction (XRD) analysis (ADVANCE-D8 model) with Cuka radiation source (λ = 1.5406 Å). Morphology of the prepared thin films were characterized by field emission scanning electron microscopy (FE-SEM) by means of a MIRA3 TESCAN- LMU electron microscope instrument and elemental combination, as well as concentrations of the films were, analyzed by energy-dispersive X-ray spectroscopy (EDX) using attached to FESEM instrument. UV–Vis optical transmittance was performed by a Perkin Elmer Lambda 25 double beam spectrophotometer. The absorption coefficient and band gap of the samples were estimated by using Beer–Lambert law and Tauc plot, respectively. According to Tauc's equation one can find the band gap of material from the following equation: [36]

$$\alpha h\upsilon = A\left(h\upsilon - E_g\right)^n$$

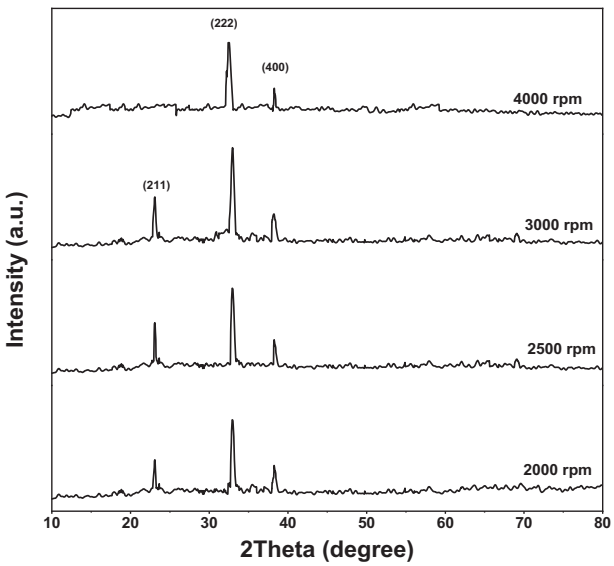

Fig. 5 XRD patterns of Mn_2O_3 thin films deposited at different spin speeds; form bottom to top: S_{2000}, S_{2500}, S_{3000}, and S_{4000} samples

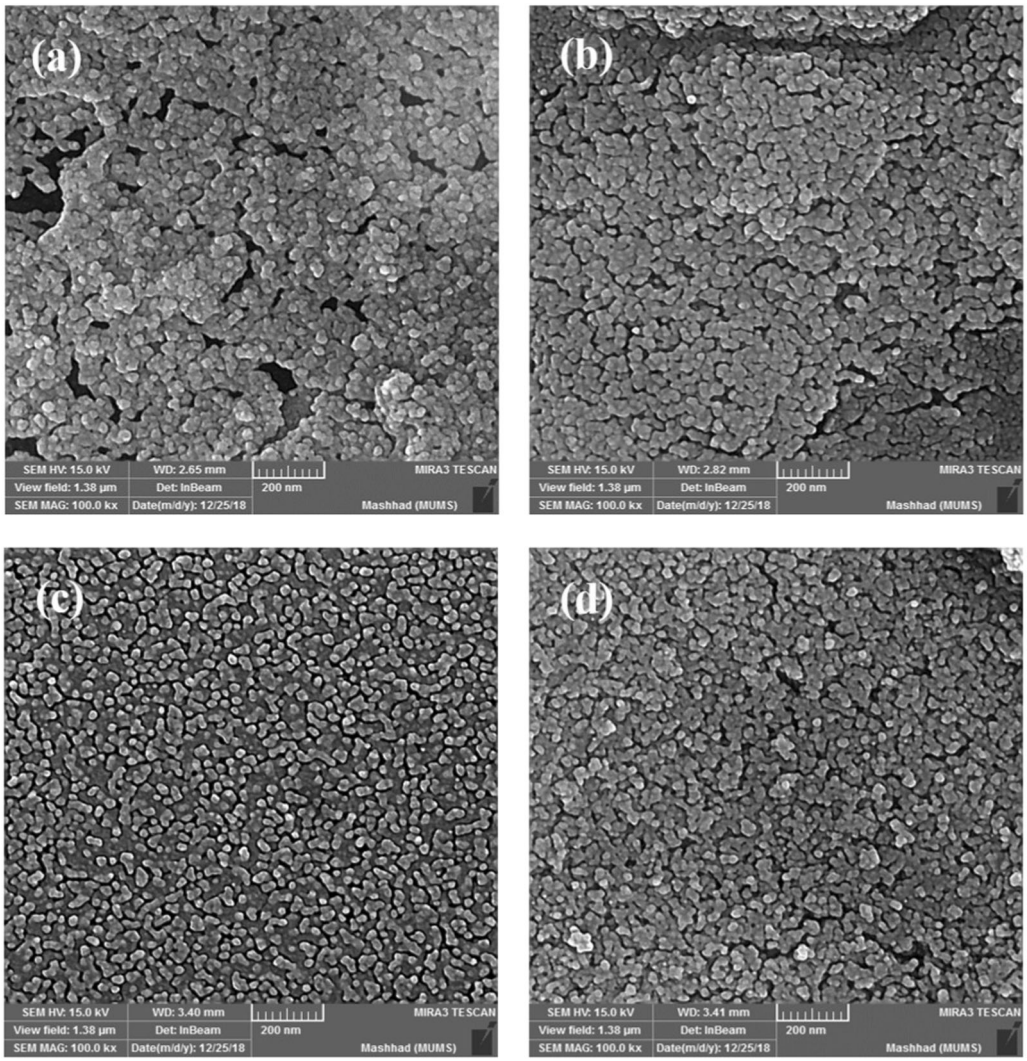

Fig. 6 SEM images of samples deposited at different spin speeds; **a** S_{2000}, **b** S_{2500}, **c** S_{3000}, and **d** S_{4000}

where α is the absorption coefficient, A is a constant, h is Planck's constant, υ is the frequency, and E_g is the band gap. The exponent n is 2 and 1/2 for indirect and direct allowed transitions, respectively. So for direct band gap material the plotying of $(\alpha h\upsilon)^2$ versus $h\upsilon$ and calculating the intersection of the linear fit and the photon energy axis, gives the value to E_g.

The crystalline size of the samples (D) was calculated by the Debye–Scherrer equation: [37]

$$D = \frac{k\lambda}{\beta \cos\theta}$$

where k is a constant, λ is the wavelength of X-rays (1.5418 Å), β is the FWHM (full width at half maximum), k is the Scherrer constant which dependent on the crystallite shape (here $k = 0.9$), and θ is the Bragg angle.

3 Results and discussion

3.1 Effect of calcination temperature

XRD analysis has been carried out, to find out the structural properties of the samples. Figure 1a shows XRD patterns of samples with 5 deposited layers and (b) shows XRD of samples with 6 layers, which calcined at different temperatures. It is clear from Fig. 1a that for relatively low calcination temperature (i.e., 400 °C) no crystalline phase has been detected. By increasing the calcination temperature to 450 °C, Mn_2O_3 phase with orthorhombic structure and *pbca* space group matching with card number of 01-071-0635, is formed. Further increasing the calcination temperate for S^6_{500} sample leads to crystallinity improvement and other crystalline planes, such as (211) and (400) can be

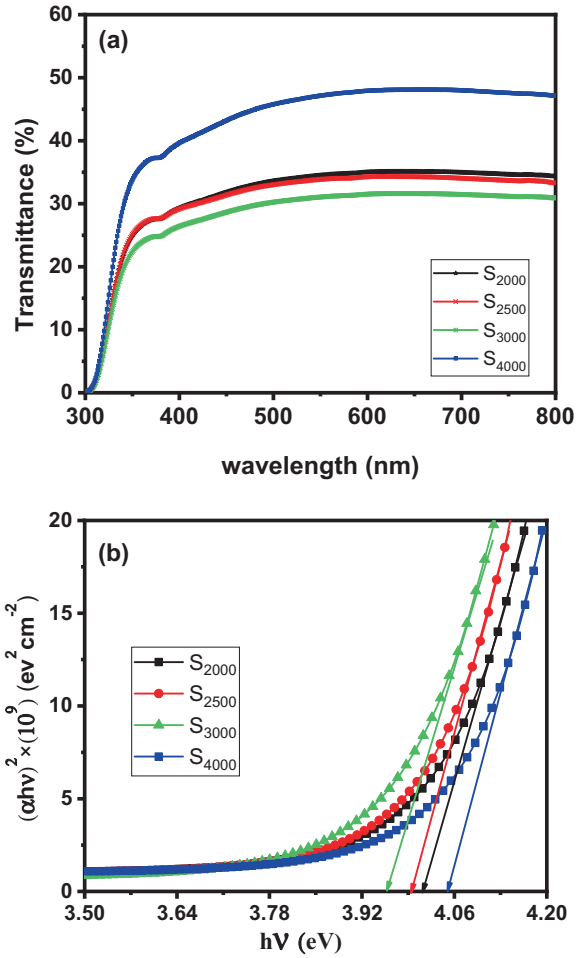

Fig. 7 **a** Optical transmittance and **b** Tauc's plot for S_{2000}, S_{2500}, S_{3000}, and S_{4000} samples

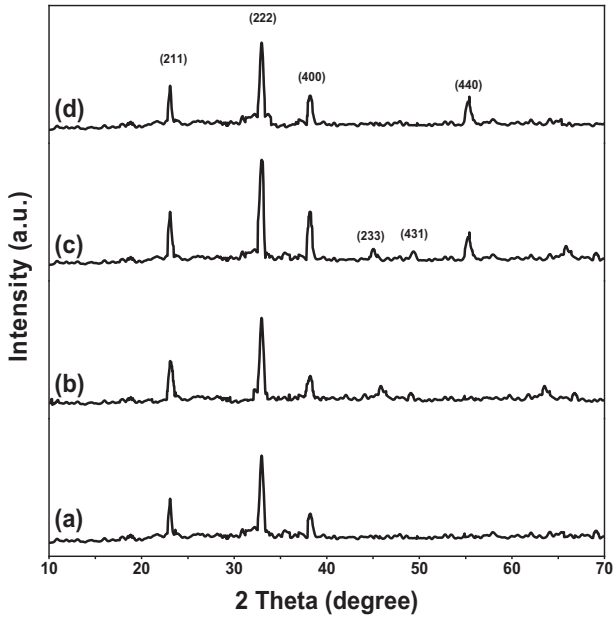

Fig. 8 XRD patterns of Mn_2O_3 thin films with different solution aging times; **a** non-aged (sample S^6_{500}), **b** 15 d, **c** 30 d, and **d** 45 d samples

detected in XRD pattern of this sample (Fig. 1b). XRD patterns revealed the [222] direction as the preferred growth orientation of the samples. By using Scherrer's equation, crystallite size of the samples was calculated as 19.3 nm, 25.2 nm, and 28.6 for S^5_{450}, S^6_{450}, and S^6_{500}, respectively. The increase in grain size may be attributed to both the layer number increment and increase of the calcination temperature.

Further investigation on structural properties and quantitative analysis of XRD patterns has been performed using Rietveld method by MAUD software refinement program, version 2.8. Figure 2 exhibits Rietveld fitting output and experimental results for S^6_{500} sample. Peak positions of orthorhombic Mn_2O_3 are marked as bar sequences below XRD patterns and difference between observed (I_o) and calculated (I_c) intensities is plotted at the bottom of the plot.

Generally, Relative agreement factors R_{wp}, which weights residual error, is used to ascertain the ability of the performed structural model to account for the experimental data [38]. The value of goodness of fit (GOF) difference between experimental data and the calculated curve is calculated using the following equation:[39]

$$\mathrm{GOF} = \frac{R_{\mathrm{WP}}}{R_{\mathrm{exp}}}$$

where R_{exp} is the expected error. An appropriate fit observed with the GOF value of 0.61 for S^6_{500} sample, notably indicates the fitting is appropriate for this nanostructured thin film. The calculated cell parameters are $a = 9.36$, $b = 9.32$, and $c = 9.39$ angstrom.

Morphological analysis of S^5_{400}, S^5_{450}, S^6_{400}, S^6_{450}, S^6_{500}, and S^7_{500} samples are presented in Fig. 3a–f. Insets 3e is the EDX analysis of that sample. At lower calcination temperatures, for both 5 and 6 layer samples, a non-uniform surface without any distinct nanostructure can be observed. In the case of the highest calcination temperature, Fig. 3f reveals that the growth mechanism changes significantly with increasing the number of layers from 5 to 6.

EDS analysis for S^6_{500} sample showed no impurity element in the layer. The obtained atomic ratio of oxygen and manganese was 69% and 31%, respectively, which is in good agreement with the predicted theoretical values for Mn_2O_3.

Fig. 4a and c exhibit transmittance spectra and Fig. 4b and d exhibit $(\alpha h\upsilon)^2$ versus $h\upsilon$ plot of 5 layer and 6 layer thin films, respectively. Results showed that by increasing the calcination temperature, the transmittance of deposited films decreased. Furthermore, by increasing the calcination temperature, band gap of the samples shifted to lower values and a red shift could be observed which indicated

formation of smaller crystallite size due to quantum confinement effect. Interestingly, considering the SEM images, one may conclude that increasing the calcination temperature has led to increase of some particles in size. In fact, it may not be the case necessarily. That is, what is observed in SEM image might be some domains which have enlarged due to aggregation of small crystallites. On the other hand, the crystallite size of the samples calculated using Scherrer's equation shows no much difference which may be an evidence of aggregation happening.

3.2 Effect of rotation speed

In this part, the effect of spin speed on physical properties of the samples has been studied. Figure 5 shows XRD patterns of S_{2000}, S_{2500}, S_{3000}, and S_{4000} samples. The calculated crystallite sizes are 19.8 nm, 19.8 nm, 28.6 nm, and 13.4 nm, respectively. This shows that for lower speeds the crystallite size did not change, while for the highest speed (i.e. 4000 rpm) the crystallite size decreased, which could be attributed to the effect of high rotation speed in preventing the uniform dispersion of the solution on the surface.

Figure 6 displays FESEM images of samples deposited at different rotation speeds. The morphology of S_{2000} sample (Fig. 6a) is not uniform. The surface is not covered by the nanoparticles as well as cracks can be seen all over the surface. The nanoparticles are more uniformly distributed for S_{2500} sample (Fig. 6b), and cracks are less than that in previous sample. S_{3000} sample showed a uniformly distributed nanoparticles without any pinhole or crack on the surface. In the case of S_{4000} sample (Fig. 6d), the spinning speed is so fast that the solution did not have the chance for uniform dispersion on the surface, so again

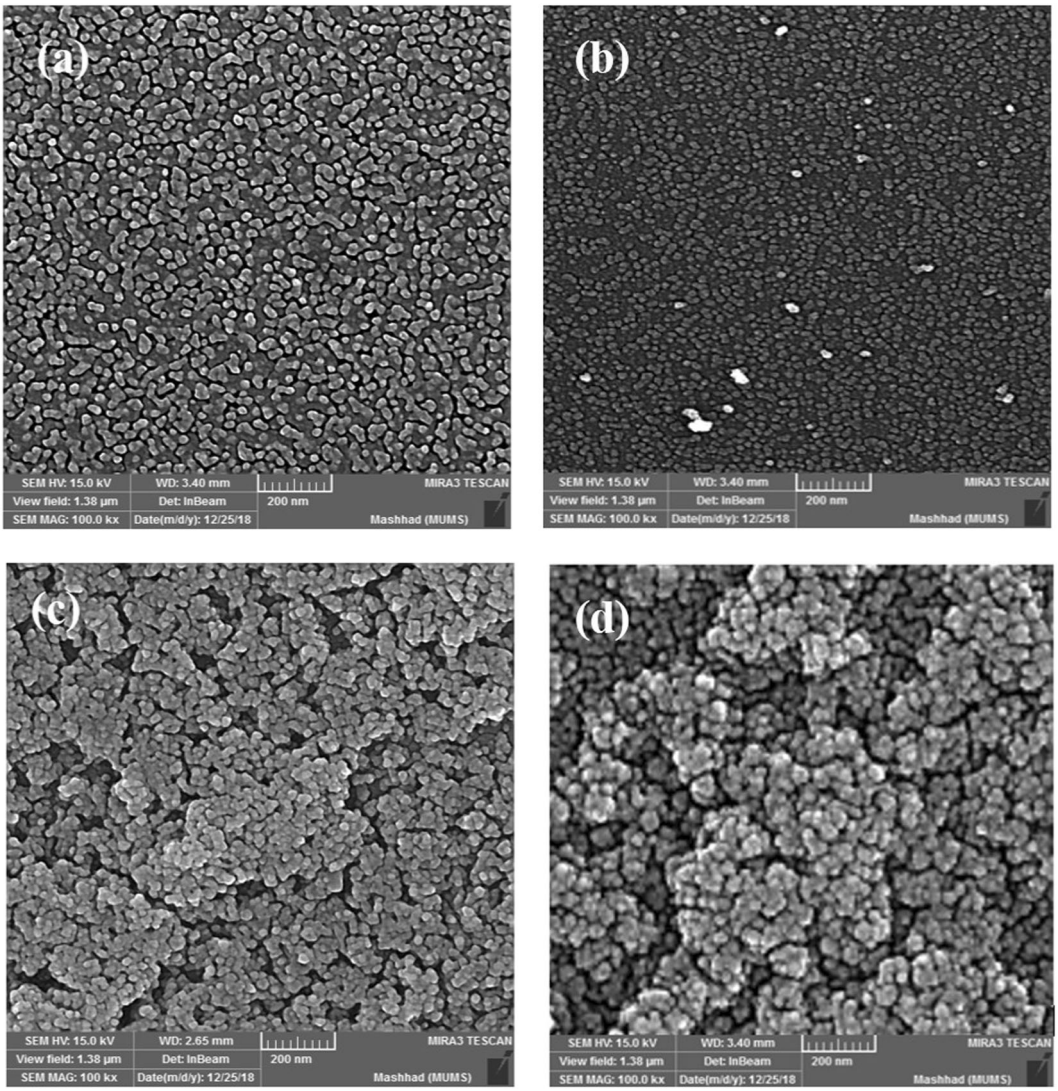

Fig. 9 FESEM images of the samples with different solution aging times; **a** non-aged (sample S^{6}_{500}), **b** 15 d, **c** 30 d, and **d** 45 d

cracks and non-uniformity in the morphology of the sample can be observed.

Optical transmittance and Tauc's plot of the samples as functions of rotation speed (for S_{2000} –S_{4000} samples) are displayed in Fig. 7a, b, respectively. High spin speed leads to more transparent thin film due to lowering the thickness of the sample. The calculated band gaps are ranging from 3.95 eV to 4.05 eV. S_{4000} shows the highest transparency and the largest optical band gap. As it is clearly seen, the transmittance decrement has led to band gap shift towards lower energies.

3.3 Effect of solution aging

At the next step, precursor solution has been aged for different periods. For this purpose, deposition conditions were selected identical to those of sample S^6_{500}. The starting solution was aged for 15, 30, and 45 days (acronyms are explained in the "Experimental" section). Results are collected and compared with non-aged (fresh) solution results. Figure 8 demonstrates the XRD patterns of the samples. Calculated crystallite sizes were 28.6 nm, 17.4 nm, 16.9, and 16.5 nm for fresh, 15 d, 30 d, and 45 d samples. The results showed that crystallite size decreased significantly with solution aging. On the other hand, some other crystallographic planes such as (233), (431), and (440) appeared upon increasing the aging time of solution.

Figure 9 represents the surface morphology of Mn_2O_3 thin films with different aging periods. It can be seen that for non-aged (Fig. 9a) and 15 d (Fig. 9b) samples small nanoparticles have been grown up. But by further increasing the solution aging time, grain-growth mechanism has been changed and surface has been composed of bigger agglomeration of nanoparticles.

Figure 10 shows the optical transmittance spectra and absorption coefficient of Mn_2O_3 thin films with different aging times. From Fig. 10a, the optical transmittance of the samples decreased about 10 percent by increasing the aging time. However, aging the solution did not change the absorption edge of the samples and according to Fig. 10b the band gap of samples with different aging times was found to be 3.92 eV.

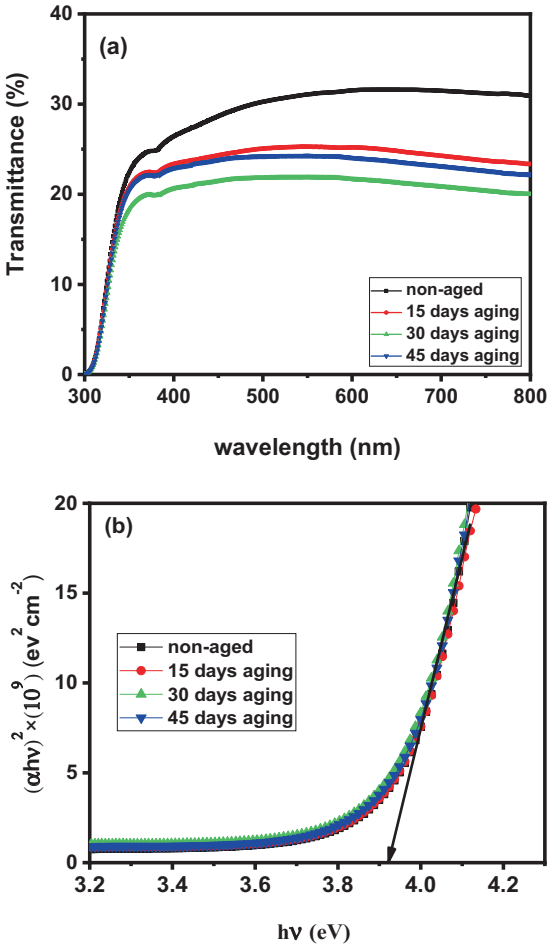

Fig. 10 Effect of the solution aging on **a** optical transmittance, and **b** Tauc's plot of Mn_2O_3 thin films

4 Conclusion

Mn_2O_3 thin films have been deposited on soda-lime glass substrates by spin coating method. The effect of calcination temperature, rotation speed, and solution aging time was studied by means of XRD, FESEM, and optical transmission spectroscopy techniques. The results showed that relatively low calcination temperature, i.e. 400°C led to amorphous thin films, while by increasing it orthorhombic phase formed. For higher rotation speeds, the crystallinity of the samples decreased since solution was not able to disperse uniformly on substrate surface. FESEM results indicated that for low calcination temperature a uniform structure was not formed and agglomerations of particles happened. It was also observed that the calcination temperature and rotation speed can significantly affect the transparency of the films and make shift in their band gap energy. Aging the solution did not change the absorption edge of the samples. However, the optical transmittance of the samples decreased about 10 percent.

Compliance with ethical standards

Conflict of interest The authors declare that they have no conflict of interest.

Publisher's note Springer Nature remains neutral with regard to jurisdictional claims in published maps and institutional affiliations.

References

1. Shaikh A, Waikar M, Sonkawade R (2019) Effect of different precursors on electrochemical properties of manganese oxide thin films prepared by SILAR method. Synth Met 247:1–9
2. Astinchap B, Moradian R, Namdari T, Jurečka S, Ţălu Ş (2019) Prepared σ-MnO_2 thin films by chemical bath deposition methods and study of its optical and microstructure properties. Optical Quantum Electron 51(6):170
3. Ahmadian H, Tehrani FS, Aliannezhadi M (2019) Hydrothermal synthesis and characterization of WO_3 nanostructures: effects of capping agent and pH. Mater Res Express 6(10):105024
4. Jamali M, Tehrani FS (2020) Effect of synthesis route on the structural and morphological properties of WO_3 nanostructures. Mater Sci Semiconductor Process 107:104829
5. Sharma S, Chauhan P, Husain S (2016) Structural and optical properties of Mn_2O_3 nanoparticles and its gas sensing properties. Adv Mater Proc 1:220–225
6. Mansouri M (2018) Effects of vacancy-defected, dopant and the adsorption of water upon Mn_2O_3 and Mn_3O_4 (001) surfaces: a first-principles study. Acta Physica Polonica A 133(5):1178–1185
7. Yang S et al. (2019) The excellent electrochemical performances of $ZnMn_2O_4/Mn_2O_3$: The composite cathode material for potential aqueous zinc ion batteries. J Electroanalytical Chem 832:69–74
8. Parveen N et al. (2019) Feasibility of using hollow double walled Mn_2O_3 nanocubes for hybrid Na-air battery. Chem Eng J 360:415–422
9. Abrego-Martínez J et al. (2019) Nanostructured Mn_2O_3/Pt/CNTs selective electrode for oxygen reduction reaction and methanol tolerance in mixed-reactant membraneless micro-DMFC. Electrochim Acta 297:230–239
10. Lee JH, Kim KJ (2013) Superior electrochemical properties of porous Mn_2O_3-coated $LiMn_2O_4$ thin-film cathodes for Li-ion microbatteries. Electrochim Acta 102:196–201
11. Sasikumar R, Chen T-W, Chen S-M, Rwei S-P, Yu M-C(2018) Facile synthesis of Mn_2O_3 for highly active catalytic oxidation and reduction of organic substances and electrochemical determination of L-methionine Int J Electrochem Sci 13(5):4561–4574
12. Korotcenkov G, Brinzari V, Ham M (2018) Materials acceptable for gas sensor design: advantages and limitations. Key Eng Mater 780:80–89
13. Hou Y, Cheng Y, Hobson T, Liu J (2010) Design and synthesis of hierarchical MnO_2 nanospheres/carbon nanotubes/conducting polymer ternary composite for high performance electrochemical electrodes. Nano Lett 10(7):2727–2733
14. Liu P-P, Zheng Y-Q, Zhu H-L, Li T-T (2019) Mn_2O_3 hollow nanotube arrays on Ni foam as efficient supercapacitors and electrocatalysts for oxygen evolution reaction. ACS Appl Nano Mater 2(2):744–749
15. Zhang X et al. (2019) Influence of hydrothermal synthesis temperature on the redox and oxygen mobility properties of manganese oxides in the catalytic oxidation of toluene. Trans Metal Chem 44:663–670
16. Bach S, Henry M, Baffier N, Livage J (1990) Sol-gel synthesis of manganese oxides. J Solid State Chem 88(2):325–333
17. Yang D (2012) Pulsed laser deposition of cobalt-doped manganese oxide thin films for supercapacitor applications. J Power Sources 198:416–422
18. Broughton J, Brett M (2004) Investigation of thin sputtered Mn films for electrochemical capacitors. Electrochim Acta 49(25):4439–4446
19. Maruyama T, Osaki Y (1995) Electrochromic properries of manganese oxide thin films prepared by chemical vapor deposition. J Electrochem Soc 142(9):3137–3141
20. Walter C, Menezes PW, Loos S, Dau H, Driess M (2018) Facile formation of nanostructured manganese oxide films as high-performance catalysts for the oxygen evolution reaction. ChemSusChem 11(15):2554–2561
21. Sarkar A, Satpati AK, Kumar V, Kumar S (2015) Sol-gel synthesis of manganese oxide films and their predominant electrochemical properties. Electrochim Acta 167:126–131
22. Nilsen O, Fjellvåg H, Kjekshus A (2003) Growth of manganese oxide thin films by atomic layer deposition. Thin Solid Films 444 (1–2):44–51
23. Komaraiah D, Radha E, Reddy MR, Kumar JS, Sayanna R (2019) Structural, optical properties and photocatalytic activity of nanocrystalline TiO_2 thin films deposited by sol–gel spin coating. i-Manager's J Mater Sci 7(1):28
24. Ziller S, von Bülow J, Dahl S, Lindén M (2017) A fast sol–gel synthesis leading to highly crystalline birnessites under non-hydrothermal conditions. Dalton Trans 46(14):4582–4588
25. Sahu N, Parija B, Panigrahi S (2009) Fundamental understanding and modeling of spin coating process: a review. Indian J Phys 83 (4):493–502
26. Maezono R, Ishihara S, Nagaosa N (1998) Phase diagram of manganese oxides. Phys Rev B 58(17):11583
27. Devaraj S, Munichandraiah N (2008) Effect of crystallographic structure of MnO_2 on its electrochemical capacitance properties. J Phys Chem C 112(11):4406–4417
28. Awad MA, Hadia NMA (2018) Towards understanding the morphological, magnetic, optical and electrical properties of MnO2 nanowires for magneto-and optoelectronic applications. J Mater Sci: Mater Electron 29(24):20695–20702
29. Augustin M et al. (2015) Manganese oxide phases and morphologies: a study on calcination temperature and atmospheric dependence. Beilstein J Nanotechnol 6(1):47–59
30. Fang Y, Wang Y, Wang F, Zhu J (2019) 3D structured Mn_2O_3 synthesized using tween surfactant: influence on the morphology and oxygen reduction catalytic performance. CrystEngComm 21 (3):420–429
31. Falahatgar S, Ghodsi F (2016) Optical characterization of nanostructured MnO_2ZnO thin films prepared from acetate-based sol−gel precursors. Opt-Int J Light Electron Opt 127 (3):1059–1065
32. Chin S-F, Pang S-C, Anderson MA (2002) Material and electrochemical characterization of tetrapropylammonium manganese oxide thin films as novel electrode materials for electrochemical capacitors. J Electrochem Soc 149(4):A379–A384
33. Fau P, Bonino J, Rousset A (1994) Electrical properties of sputtered MnO_2 thin films. Appl Surf Sci 78(2):203–210
34. Pang SC, Chin SF, Ling CY (2011) Preparation and characterization of self-assembled manganese dioxide thin films. J Nanotechnol 2011:789305
35. Hernández S et al. (2016) Spin-coated vs. electrodeposited Mn oxide films as water oxidation catalysts. Materials 9(4):296
36. Hassanien A, Akl AA (2016) Effect of Se addition on optical and electrical properties of chalcogenide CdSSe thin films. Superlattice Microst 89:153–169
37. Aawani E, Memarian N, Dizaji HR (2019) Synthesis and characterization of reduced graphene oxide–V_2O_5 nanocomposite for enhanced photocatalytic activity under different types of irradiation. J Phys Chem Solids 125:8–15
38. Venkatramu V et al. (2010) Nanocrystalline lanthanide-doped $Lu_3Ga_5O_{12}$ garnets: interesting materials for light-emitting devices. Nanotechnology 21(17):175703
39. Sain S, Patra S, Pradhan S (2012) Quickest ever single-step mechanosynthesis of $Cd_{0.5}Zn_{0.5}S$ quantum dots: nanostructure and optical characterizations. Mater Res Bull 47(4):1062–1072